Eur. Phys. J. B **6**, 487–496 (1998)

THE EUROPEAN PHYSICAL JOURNAL B

X-ray spectroscopy of the metal-insulator transition in $Yb_{1-x}Gd_xTe$ and $Yb_{1-x}La_xTe$

S. Merah[1], D. Ravot[1,2], A. Mauger[3,a], A. Percheron-Guégan[1], J.C. Dumas[2], J. Olivier-Fourcade[2], and O. Gorochov[4]

[1] Laboratoire de Chimie Métallurgique des Terres Rares, Centre National de la Recherche Scientifique, 1 place A. Briand, 92195 Meudon Cedex, France
[2] Laboratoire de Physico-Chimie de la Matière Condensée, Université des Sciences et Techniques du Languedoc, place Eugène Bataillon, 34095 Montpellier Cedex 5, France
[3] Laboratoire des Milieux Désordonnés et Hétérogènes, Université Pierre et Marie Curie, 4 place Jussieu, 75251 Paris Cedex 05, France
[4] Laboratoire de Physique des Solides, Centre National de la Recherche Scientifique, 1 place A. Briand, 92195 Meudon Cedex, France

Received: 23 March 1998 / Revised and Accepted: 12 July 1998

Abstract. We report extended X-ray absorption fine structure (EXAFS) of $Yb_{1-x}Gd_xTe$ and $Yb_{1-x}La_xTe$, two solid solutions which show an insulator-metal transition (IMT) as a function of x for a high donor concentration $x_c \approx 0.2$. The results are correlated to transport experiments and X-ray diffraction data, to analyse the IMT in relation to the structure at both a local and a macroscopic scale. A bimodal distribution is found for rare earth-Te nearest distances in these compounds crystallized in the fcc structure. In particular, we find the less rigid Yb–Te bond can be used as a local probe for the wavefunction of the electrons introduced by La or Gd donors, hence a new insight on the metal-insulator transitions which are of a different nature in the two solid solutions.

PACS. 71.30.+h Metal insulator transitions and other electronic transitions – 61.10.Ht X-ray absorption spectroscopy: EXAFS, NEXAFS, XANES, etc.

1 Introduction

Rare-earth monotellurides crystallize in the fcc structure. Among them, YbTe is a large gap semiconductor, as both tellurium and ytterbium are divalent. Upon doping with a trivalent rare earth ion acting as a donor, one can then add up electrons which, at high enough concentrations, will drive a transition into a metallic state. Among them Gd^{3+} and La^{3+} ions are of particular interest. First, Gd^{3+} carries a spin $S = 7/2$, while Yb^{2+} is diamagnetic. As a consequence, YbTe is non-magnetic, while GdTe is a type-II antiferromagnet with Néel temperature $T_N = 76$ K. Therefore, the solid solution $Yb_{1-x}Gd_xTe$ undergoes not only a insulator-metal transition (IMT), but also a magnetic transition as a function of x. Indeed, we have used this solid solution as an archetype to investigate the role of magnetic fluctuations on the IMT [1,2]. We have argued that the long-range magnetic order is replaced by a spin glass phase at Gd concentration $x_m = 0.5$, while the IMT takes place at $x_c = 0.22 \pm 0.03$. The range $x_c < x < x_m$ is a pre-transitional regime characterized by anomalous transport properties related to magnetic fluctuations in the metallic state [1,2].

On another hand, La^{3+} is non-magnetic. Indeed $Yb_{1-x}La_xTe$ is diamagnetic in the whole range $0 < x < 1$. We can then expect that a direct comparison between $Yb_{1-x}Gd_xTe$ and $Yb_{1-x}La_xTe$ will allow us to isolate the magnetic effects on the IMT, using $Yb_{1-x}La_xTe$ as the non-magnetic reference. From electric resistivity measurements, we have found that x_c is about the same in both solid solutions. This is quite a surprising result, as one would have expected that the magnetic interactions, which do affect the transport properties in the vicinity of the IMT in $Yb_{1-x}Gd_xTe$, would also have modified x_c. In particular, x_c is one order of magnitude larger than the value predicted by the Mott criterium $n_c^{1/3}a_B = 0.25$, where n_c is the electron concentration at the IMT, and a_B the Bohr radius of the electron orbital on the donor.

In the case of $Yb_{1-x}Gd_xTe$, one can invoke the magnetic polaron effect to explain such a large value of x_c. The basic idea is that the Gd^{3+} ions in the neighborhood of a donor are spin-polarized by the exchange interaction with the electron in excess on the donor. The magnetic exchange energy won in the spin polarization process

[a] e-mail: mauger@aomc.jussieu.fr

contributes to the binding energy, hence a shrinking of the orbital of the electron bound to the donor. The magnetic polaron formed by the donor electron surrounded by the cloud of spin polarization is then localized up to a donor concentration so large that the radius of the electron compares with the average mean distance between Gd^{3+} ions. Such a concentration is approximatively given by the Mott formula, with, however, a_B substituted by the smaller radius of the electron orbital in the bound magnetic polaron state.

The same argument does not apply to $Yb_{1-x}La_xTe$, as the material is non-magnetic. Actually, one would have expected x_c to be reduced to the per cent, in agreement with the Mott criterium in this case. The fact that x_c is the same in $Yb_{1-x}La_xTe$ and $Yb_{1-x}Gd_xTe$ is then a paradox. One purpose of the present work is a better understanding of this paradox.

The properties giving information only at a macroscopic scale, such as magnetization curves, x-dependence of the lattice parameter, electric resistivity curves [1–3], are of little help for this purpose. Properties at a microscopic scale are needed. This was the motivation for Extended X-ray Absorption Spectroscopy (EXAFS) experiments, we report in this paper. In the EXAFS domain between 50 to 1000 eV after the absorption edge, the photoelectron ejected during the absorption process has a kinetic energy of some tens of hundreds of electron volts. This gives photoelectrons a mean free path of typically 4–6 Å arising from the finite lifetime of the excited state and makes EXAFS an adequate local probe. In simple magnetic semiconductors obtained by introducing Mn ions in II–VI compounds, the lattice parameter varies linearly as a function of the magnetic ion concentration x. Even in such ideal solid solutions where the Vegard's law applies, does the EXAFS analysis reveal that, at a microscopic scale, the cation-anion distance between nearest neighbors (nn) is independent of x [4,5]. A bimodal distribution of nn distances has been also evidenced in other materials [6–11], including mixed salts [6–8] which have the same average fcc structure $Yb_{1-x}Gd_xTe$ and $Yb_{1-x}La_xTe$. These solutions are far from ideal, as the x-dependence of the lattice parameter a reported in Figure 1 shows strong deviations with respect to the Vegard's law near x_c. One can then wonder whether this deviation corresponds to changes in the anion-cation bond length. It is also the purpose of this work to answer this question.

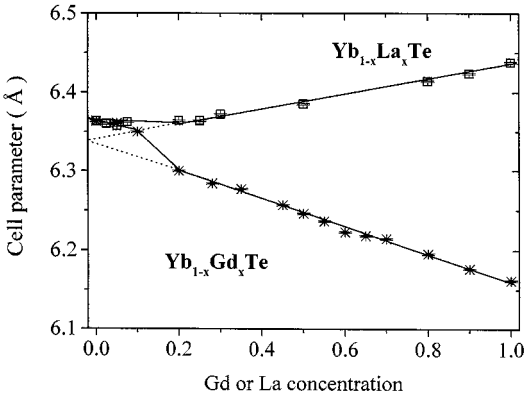

Fig. 1. Unit cell parameter a as a function of x in $Yb_{1-x}Gd_x$ and $Yb_{1-x}La_xTe$.

2 Experimental

Single crystals of the solid solutions have been obtained by direct reaction between the elements in arc-welded molybdenum crucibles, under argon atmosphere. Then the samples have been pounded to a 20 μm powder enclosed by kapton under argon atmosphere to avoid any air contamination. Room temperature EXAFS experiments have been performed at LURE (Orsay) at the L_{III} edges of the rare earths, the energies of which are $E_0 = 5483$, 6970, 8937 and 7243 eV for La, Eu, Yb, and Gd, respectively. Pure Cu sample was used for calibration. The monochromator was a (111) Si double crystal, and the broadening of the spectra by convolution with the instrumental function does not exceed 1 eV. The spectra were recorded from 63, 70, 87, and 342 eV before the edge for La, Eu, Yb, and Gd, respectively, up to 400, 630, 863, 647 eV after it, respectively. Except for Yb, the upper limit of the energy range is chosen in order to avoid L_{II} thresholds: $E_0(L_{II}) = 5891$, 7610, 7923 eV for La, Eu and Gd. In this energy range, the average discrimination in energy is better than 10^{-4}. The data have been recorded by 2 eV energy steps, and counting time was 2 seconds. The result is illustrated in Figure 2 at La, Gd thresholds, and at the Yb threshold of the $Yb_{1-x}Gd_xTe$ solution. The reduction process of the EXAFS spectra has been made according to the procedure described in reference [12], adapted to PC's environment [13]. First, the pre-edge contribution is fit by a second-order polynomial and subtracted from the total absorption. Above the edge, the absorption coefficient $\mu(E)$ contains both the isolated atom contribution $\mu_0(E)$ and the structural contribution. $\mu_0(E)$ is computed as the smooth part of $\mu(E)$ after the edge, and then subtracted from $\mu(E)$ to deduce the relative variation of the absorption coefficient with respect to that of the free absorbing atom: $\chi(E) = (\mu_0(E) - \mu_0(E))/\mu_0(E)$. This interference function corresponding to the data in Figure 2 is reported in Figure 3 as a function of the wavevector k defined by $E = E_0 + \hbar^2k^2/(2m)$. Then the Fourier transform

$$\chi(r) = \int_{k_m}^{k_M} W(k)k^3\chi(k)e^{-2ikr}dk \qquad (1)$$

is computed. The weighting factor k^3 is chosen to overcome the damping of the EXAFS oscillations at large wavevectors k. $W(k)$ is a Kaiser-type window, which differs from the Heavyside function by the smoothening of the jumps between 0 and 1 at the cuts-off k_m and k_M, over a range the order of 1 $Å^{-1}$ to avoid spurious oscillations in $\chi(r)$. $k_M > 10$ $Å^{-1}$. The cut-off vector k_m has to be chosen large enough, so that the multiple diffusions (neglected in the EXAFS analysis) are indeed negligible. Actually, the multiple scattering is enhanced by focusing effect of collinear configurations, as rare earth – Te – rare

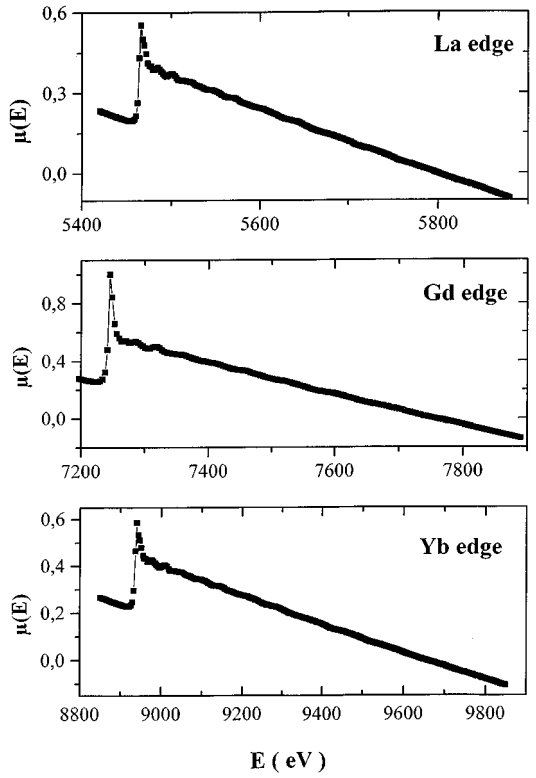

Fig. 2. Unfiltered absorption coefficient as a function of the energy near La, Gd and Yb L_{III}-thresholds in $Yb_{0.1}La_{0.9}Te$, $Yb_{0.5}Gd_{0.5}Te$ and $Yb_{0.4}Gd_{0.6}Te$, respectively.

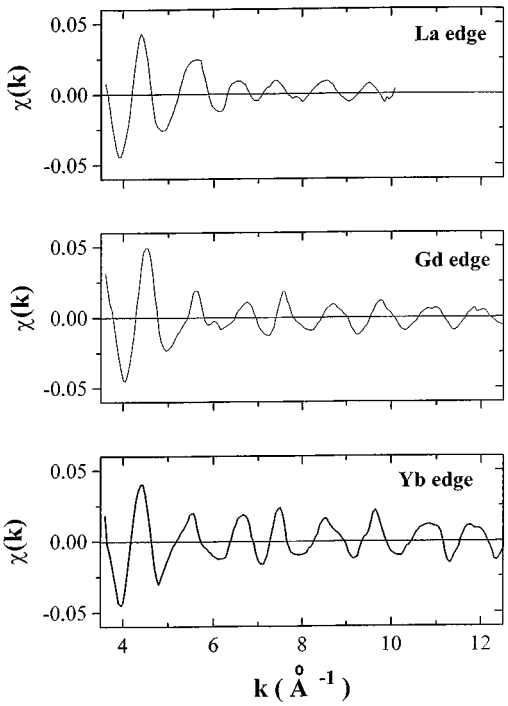

Fig. 3. Unfiltered EXAFS interference function χ as a function of the wavevector k of the photoelectron, for the same edges and same solid solutions as in Figure 2.

earth in our case. We have checked that the fits of the EXAFS data with the same k_M, but two different k_m, namely $k_m = 3.6$ and 4.5 Å^{-1}, gives the same distances, which is the proof that the multiple scattering is negligible, and does not affect EXAFS data in the range 3.6–4.5 Å^{-1}, and *a fortiori* at larger k vectors. Therefore, k_m has been taken equal to 3.6 Å^{-1}. This value amounts to an energy 50 eV larger than that of the threshold in the absorption spectra. Interatomic distances can be distinguished provided they differ by more than $(k_M - k_m)^{-1} \approx 0.16$ Å. Then, we can separate between contributions $\chi_j(r)$ of the jth shell at distance r_j from the absorber and write:

$$\chi(r) = \sum_j \chi_j(r).$$

In practice, the $\chi(r)$ curve is characterized by a large peak corresponding to the first rare earth-tellurium pair, followed by smaller peaks more difficult to separate from the background. Therefore, attention has been focussed on this first pair only. Then $\chi_j(k)$ is computed by Fourier transform

$$\chi_j(k) = \frac{1}{2\pi} \int_{r_m}^{r_M} W_j(r)\chi_j(r)e^{ikr}dr \qquad (2)$$

with $W_j(r)$ the window function associated to the cut-off distances r_M and r_m on both sides of the peak in $\chi(r)$ associated to jth contribution. $\chi_j(k)$ is the function which is fit in the analysis process, and compared with its theoretical expression (14):

$$\chi_j(k) = S_0^2 \frac{N_j}{kr_j^2} e^{(-\frac{2r_j}{\lambda})} e^{(-2\sigma_j^2 k^2)} |f_j(k)| \sin[2kr_j + \Phi_j(k)] \qquad (3)$$

N_j is the coordination number for the jth shell.

In the following, it is understood that we deal with the nn pair rare earth – tellurium only, and we shall omit the index j, to simplify the notations. The mean free path λ of the electron in the material enters an exponential associated to the loss of coherence due to inelastic scattering. σ is the Debye-Waller coefficient. $|f(k)|$ is the amplitude of the backscattered wavefunction and Φ is the phase shift of the absorber – diffusing center pair: $\Phi(k) = 2\delta_1(k) + \arg[f(k)]$, with $\delta_1(k)$ the phase shift, which only depends on the nature of the absorber. First, $|f(k)|$ and $\phi(k)$ functions have been determined on the unsubstituted compounds, by a recurrence procedure: the EXAFS spectrum of the reference compound is fit, with σ and λ the fitting parameters. At the initial step, the amplitude function and the phase shift are set to their theoretical value given in reference [15] as an input to determine the starting value of σ and λ from equation (3), other parameters being fixed by the structural information deduced from powder X-ray diffraction: $N = 6$ for nearest neighbours, and $r = a/2$, with a the lattice parameter. This set (σ, λ) is then used as an input to fit the experimental interference function according to equation (3), with $|f(k)|$ and $\Phi(k)$ the fitting parameters.

In practice, the very good agreement between equation (3) and the experimental interference function thus achieved allows us to stop the recurrence process at this step.

Table 1 gives the parameters relative to the fit of the interference function for substituted compounds. Both $|f(k)|$ and $|\Phi(k)$ values have been taken equal to their values for unsubstituted compounds. In the fitting procedure, a shift of the photoelectron energy E_0 was also made possible. Note the location of the peak in the amplitude of $\chi(r)$ depends on the nature of the rare earth-Te pair, so that the r_m and r_M parameters differ from one pair to another.

The efficiency of the X-ray absorption by the target atom is slightly smaller than 100%, hence a passive electron amplitude reduction factor S_0^2 in equation (3). In our experiments, however, the target atom is the same in the unsubstituted compound and in the solid solution, so that S_0 is independent of the composition x. Therefore, this parameter does not affect the variations of the distances and Debye-Waller factors for a given nn atom pair, relative to their values in the reference compound, and it has been set equal to unity.

The same analysis on independent set of data recorded for the same sample leads to the same interatomic distances within ± 0.01 Å. We then estimate this is the uncertainty of the distances reported in this work, due to the statistical errors. As for the Debye-Waller factor, the dispersion of the values we have obtained in the process is 0.003 Å. To estimate systematic errors, a quality factor

$$f = \frac{\sum_k [k^3\chi(k)_{exp} - k^3\chi(k)_{th}]^2}{\sum_k [k^3\chi(k)_{exp}]^2}$$

has been determined at each run. The suffixes "exp" and "th" refer to experimental and theoretical value, respectively. For all the spectra, we found $f < 2\times10^{-3}$. Note the substitution in the solid solutions concern the rare earth only, so that the number of Te atoms remains equal to $N = 6$ for the nn shell of any rare earth atom in the material. Therefore, not only $|f(k)|$ and Φ, but also N are fixed parameters. This feature is important, as it breaks the correlation between σ and the amplitude of the interference function, which made possible the determination on σ in this work.

3 The EXAFS results

The amplitude $F(r) = |\chi(r)|$ of the EXAFS function weighted by k^3 according to equation (1) is reported in Figures 4–7 for several compositions x in $Yb_{1-x}Gd_xTe$ and $Yb_{1-x}La_xTe$, respectively, at the thresholds L_{III} of Yb and Gd or La. The peaks correspond to apparent interatomic distances, identified by vertical lines in the figures, uncorrected for central and backscattering phase shifts. Since the rare earths and tellurium atoms have almost the same atomic number Z, the back-scattered wavefunctions of the photoelectron issued by these atoms are very similar. The consequence is a Ramsauer-Townsend effect [16], namely in this case a splitting of the main peak associated to the rare earth – tellurium pair. This effect is evidenced by the existence of a secondary peak in $\chi(r)$ curves at a distance about 0.5 Å shorter than the main Yb–Te and Gd (La)–Te nn peaks in Figures 4–7. The Ramsauer-Townsend effect is most prominent for $\chi(r)$ measured at the L_{III} threshold of La, because the atomic number of La is closest to that

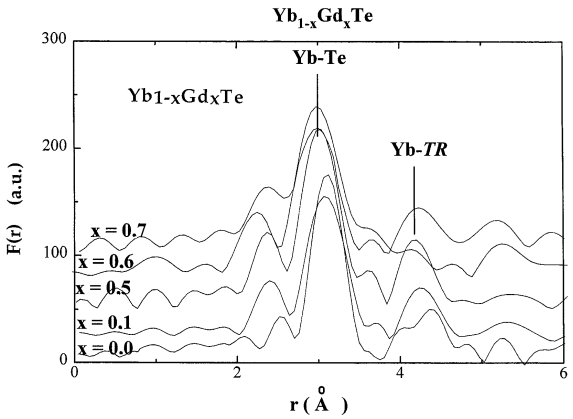

Fig. 4. Fourier transforms of the EXAFS (weighted by k^3) at room temperature, at the L_{III} thresholds of Yb in $Yb_{1-x}Gd_xTe$.

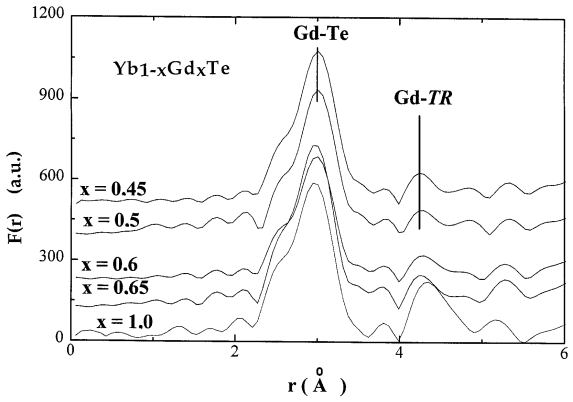

Fig. 5. Fourier transforms of the EXAFS (weighted by k^3) at room temperature, at the L_{III} threshold Gd in $Yb_{1-x}Gd_xTe$.

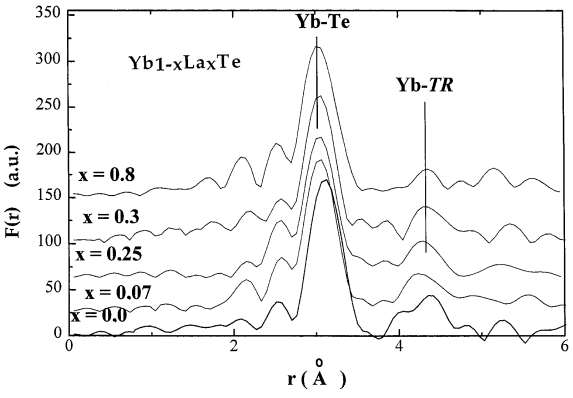

Fig. 6. Fourier transforms of the EXAFS (weighted by k^3) at room temperature, at L_{III} thresholds of Yb in $Yb_{1-x}La_xTe$.

Table 1. Input parameters for the fit of EXAFS in solid solutions are deduced from the fit of the EXAFS in the reference compounds, with r_m and r_M the cut-off distances for the window-function entering equation (2). a is the lattice parameter, and σ_{Te} the Debye-Waller coefficient for the rare earth–Te bond.

System	Absorber Atom	Reference Compound	$R_m - r_m$ (Å)	$a/2$ (Å)	σ_{Te} (Å)
Yb(Eu)Te	Yb	YbTe	2.086 – 3.620	3.180	0.080
	Eu	EuTe	2.500 – 3.850	3.300	0.018
Yb(Gd)Te	Yb	YbTe	2.086 – 3.620	3.180	0.080
	Gd	GdTe	2.148 – 3.436	3.081	0.056
La(Gd)Te	La	LaTe	2.025 – 3.988	3.219	0.062
	Gd	GdTe	2.148 – 3.436	3.081	0.056
Yb(La)Te	Yb	YbTe	2.086 – 3.620	3.180	0.080
	La	LaTe	2.025 – 3.988	3.219	0.062

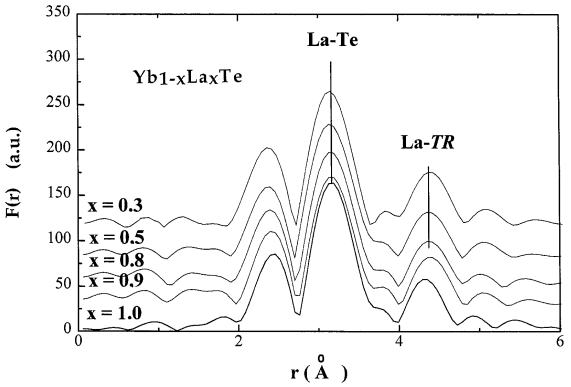

Fig. 7. Fourier transforms of the EXAFS (weighted by k^3) at room temperature, at L_{III} thresholds of La in $Yb_{1-x}La_xTe$.

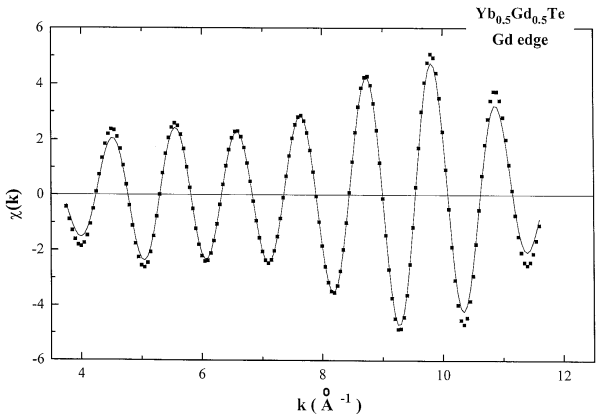

Fig. 8. Gd–Te pair contribution to the interference function for the EXAF spectra of $Yb_{0.5}Gd_{0.5}Te$ at the Gd L_{III}-edge at room temperature (■) and its fit (full curve) according to equations (2, 3) in the text.

of Te ($\Delta Z = 5$). The peaks associated to the shells of nearest (nn) and next to nearest (nnn) atoms of Yb are clearly identified. In our fcc solid solutions, the first nn shell consists in $N = 6$ Te atoms, while the nnn shell consists in 12 rare-earth atoms (Yb, Gd or La, depending on the nature of the solid solution and L_{III} threshold studied). By inverse Fourier transform of the nn shell contribution to $\chi(r)$, the contribution to the total EXAFS signal $\chi(k)$ is obtained, and reported in Figures 8–11 in $Yb_{0.5}Gd_{0.5}Te$ and $Yb_{0.2}La_{0.8}Te$ respectively, chosen as examples to illustrate the quality of the fit.

The interatomic distances and the Debye-Waller factor are then determined by fitting procedure. The results are reported as a function of x in Figures 12 and 13. In the ideal fcc structure, the rare earth–Te nearest distance is unique and equal to $a/2$, with a the lattice parameter measured from the X-ray diffraction pattern. Figures 12, 13, however, show that the Yb–Te and the (Gd,La)–Te nn distances are distinct. In addition, their x-dependence is quite different from that of the lattice parameter in Figure 1.

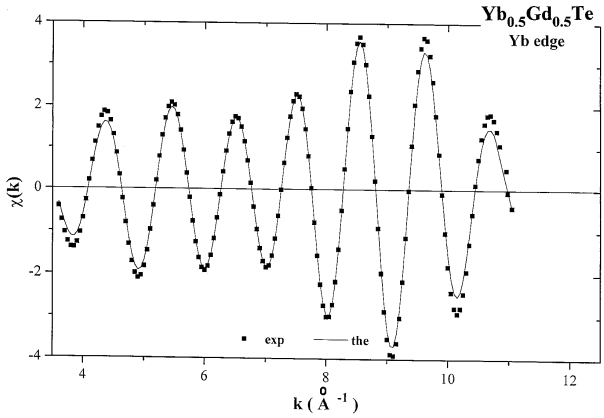

Fig. 9. Yb–Te pair contribution to the interference function for the EXAF spectra of $Yb_{0.5}Gd_{0.5}Te$ at the Yb L_{III}-edge at room temperature (■) and its fit (full curve) according to equations (2, 3) in the text.

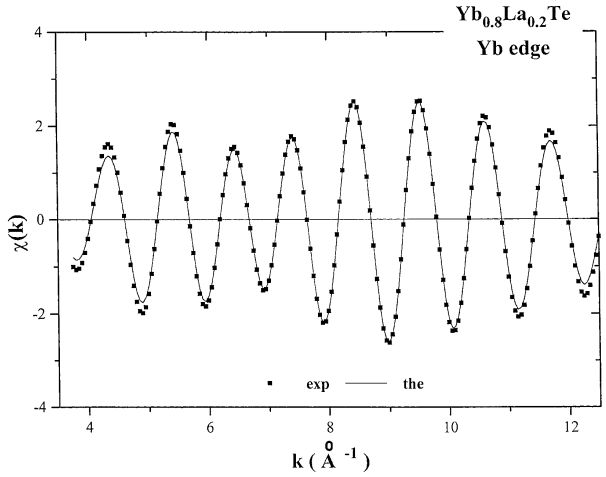

Fig. 10. La–Te pair contribution to the interference function for the EXAF spectra of $Yb_{0.2}La_{0.8}Te$ at the La LIII-edge at room temperature (■) and its fit (full curve) according to equations (2, 3) in the text.

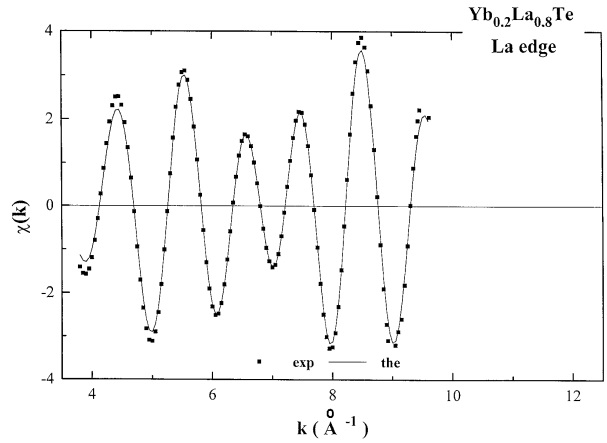

Fig. 11. Yb–Te pair contribution to the interference function for the EXAF spectra of $Yb_{0.2}La_{0.8}Te$ at the Yb L_{III}-edge at room temperature (■) and its fit (full curve) according to equations (2, 3) in the text.

4 Analysis

Starting from the metallic side in Figure 1, *i.e.* from $x = 1$, we find the lattice parameter a deduced from X-ray diffraction experiments is a linear function of x in the range $1 \leq x \leq 0.2$ for both solid solutions $Yb_{1-x}Gd_xTe$ and $Yb_{1-x}La_xTe$. Moreover, for both solutions, the straight lines $a(x)$ extrapolate to the same value at $x = 0$, namely 6.337 Å. One can then consider this is the lattice parameter YbTe would have if it were metallic, and we shall call it a_m(YbTe). However, there is an important change of slope in $a(x)$ curves at $x = 0.2$, which suggests that the metallic character is no longer retained, and indeed, the lattice parameter in the large gap semiconductor YbTe is 6.360 Å. This anomalous behavior in the $a(x)$ curves suggests the metal-insulator transition takes place, at $x \approx 0.2$ in both solid solutions.

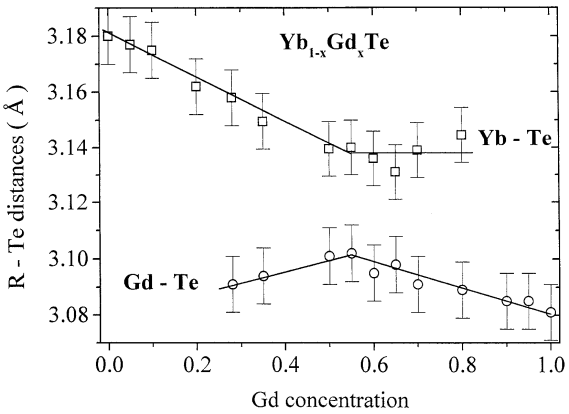

Fig. 12. x-dependence of Te–rare earth nearest distance, deduced from EXAFS (squares and circles, with error bars) for $Yb_{1-x}Gd_xTe$.

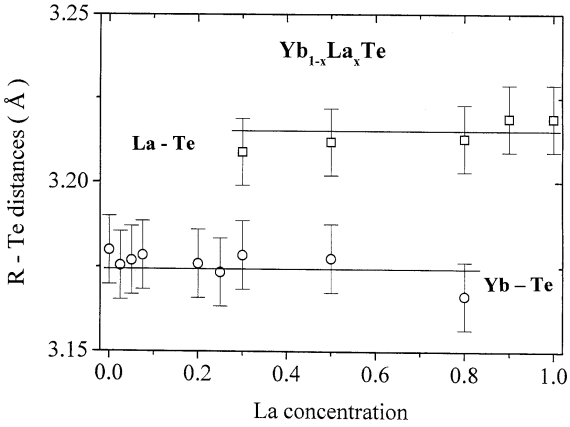

Fig. 13. x-dependence of Te–rare earth nearest distance, deduced from EXAFS (squares, with error bars) for $Yb_{1-x}La_xTe$.

This result is corroborated by transport experiments. Resistivity measurements [1–3] have shown that the solid solutions are metallic for $x > 0.2$, and the Hall effect measurements in the temperature range $77 < T < 300$ K confirm that the free electron concentration is temperature independent and close to $4x/(a^3)$. On another hand, for $x \leq 0.2$, Hall effect measurements show an activated regime for the variation of the electron concentration n as a function of $1/T$ in the same temperature range $77 < T < 300$ K. This is illustrated in Figures 16 and 17 for both solid solutions. The change in the slope of the x-dependence of the lattice parameter at $x \approx 0.2$ in Figure 1 is then unambiguously due to the IMT, both in $Yb_{1-x}Gd_xTe$ and $Yb_{1-x}La_xTe$.

EXAFS analysis reveals a bimodal distribution of nn distances, although the X-ray diffraction pattern is that of the fcc structure. In these solutions, the x-dependence of the nn distances is also affected by the IMT, which raises the question of how to separate the structural effects from the electronic effects in Figures 12 and 13. To solve this problem, we can use the EXAFS investigation of the solution $Yb_{1-x}Eu_xTe$: as Eu is divalent, just as Yb, the substitution does not induce any IMT in this case.

The counterpart of Figures 2–5 is displayed in Figure 1 of reference [3] for $Yb_{1-x}Eu_xTe$. It shows this is an ideal solution in the sense that the lattice parameter deduced from the X-ray diffraction data now satisfies the Vegard's law at any x; still, however, the distribution in nn distances is bimodal. This feature is then uncorrelated with the electron concentration in the solid solutions.

A bimodal distribution in nn distances has already been observed in Mn-based magnetic semiconductors in a II–VI host matrix crystallized in the zinc blende structure [5], and in materials of the chalcopyrite type [17]. In these cases also, a crystallographic order is observed without any superstructure, although the nn bond length is bimodal, and independent of x. The extension of the analysis in references [5–17] to our case is straightforward. The lattice parameter as deduced from X-ray diffraction data is averaged over many anion and cation sites, while EXAFS give structural details on the topologic environment of one anion and one cation. The bimodal distribution revealed by EXAFS then implies that the fcc lattice is kept only on the average, while the coordination octahedrons which constitute the frame units of the lattice have to suffer local distortion. As the cations all have the same nn anion (Te) environment, we expect that they stay on the fcc lattice site, *i.e.* in the center of the octahedron. The distortion is then due to the local motion of Te anions, which are forced to leave the center of the coordination octahedron to accommodate the presence of two different cations (rare earths) in the ternary solid solutions. As the distribution of the rare earths on the vertices of the octahedron is random [18], so is the departure of Te anions from the center of the octahedra. Therefore, the fcc structure is kept on the average, hence the appropriate X-ray diffraction pattern. This basic idea may be useful to understand the existence of local distortions, but it fails to give the actual structure of the material. The knowledge of the structure resulting from the local distortions requires a more complete study including multiple scattering contributions to probe the structure at longer distances. The reference for such an analysis is the beautiful work of Frenkel *et al.*, who solved the structure of disordered mixed salts [8]. In this case, a root mean-square buckling angle deviation from the NaCl structure has been evidenced. This result might also apply to the materials investigated in the present work, inasmuch as they have the same *average* NaCl fcc structure.

The nn Yb–Te distance in metallic $Yb_{1-x}Gd_xTe$ is independent of x for $x \geq 0.5$, and equal to 3.14 Å. This value is comparable, but smaller than $a_m(\mathrm{YbTe})/2 = 3.169$ Å, which shows that the Yb–Te bonding is affected by the presence of Gd ions. Another effect of the Gd environment is the decrease of the Yb–Te bond length with x in the range $0.2 < x < 0.5$, in Figure 12. A singularity, or at least a maximum in the nn Gd–Te distance at $x = 0.5$ is likely in the variations of the Gd–Te bond length as a function of x. This is consistent with the break in the slope of the Yb–Te bond length at the same composition, and it will be discussed later in the paper. At this stage of the analysis, it is sufficient to note that in the whole range

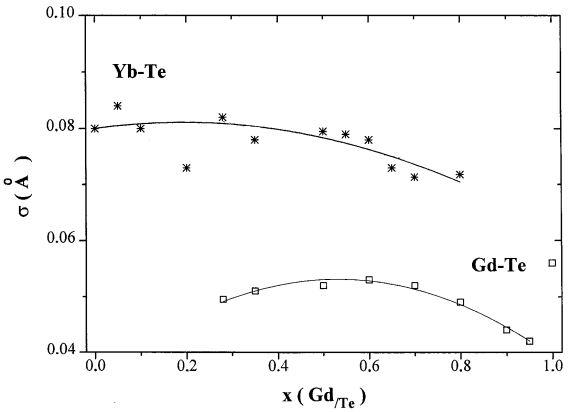

Fig. 14. Debye-Waller factor for the Gd–Te bond and the Yb–Te bond as a function of the composition x in $Yb_{1-x}Gd_xTe$.

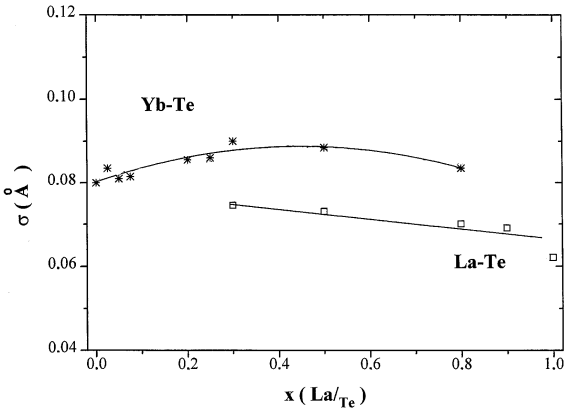

Fig. 15. Debye-Waller factor for the La–Te bond and the Yb–Te bond as a function of the composition x in $Yb_{1-x}La_xTe$.

$0.2 < x < 1$, the variation of the Gd–Te bond length is actually very small, as it does not exceed the uncertainty $\pm$ 0.01 Å in the determination of this distance (not determined for $x < 0.25$, because the Gd contribution to EXAFS spectra becomes too small). Therefore, the Gd–Te distance is almost independent of x in the metallic phase, and close to its value 3.08 Å in pure GdTe, so that the Yb ions have only little effect on the nn Gd–Te distance. This gives evidence that the Gd–Te bond is more rigid than the Yb–Te bond. This is corroborated by the Debye-Waller factors σ_{Te} for the Yb–Te and Gd–Te bonds deduced from the EXAFS analysis at L_{III} thresholds of Yb and Gd. In YbTe and GdTe compounds, the Debye-Waller coefficients are due to thermal vibrations only. In $Yb_{1-x}Gd_xTe$, a contribution of static disorder is expected. This static contribution, however is very small, since the x-dependence of σ_{Te}, reported in Figure 14 is negligible: except for a value $\sigma_{\mathrm{Te}} = 0.056$ larger than expected in the GdTe compound, σ_{Te} for the Gd–Te bond is in the range 0.04–0.05 Å in $Yb_{1-x}Gd_xTe$ at any $x \neq 0$, while it is significantly larger, in the range 0.07–0.08 Å for the Yb–Te bond at any x. Therefore, the larger value of σ_{Te} for the Yb–Te bond is due to larger thermal vibrations, another evidence of the weaker nature of the Yb–Te bond.

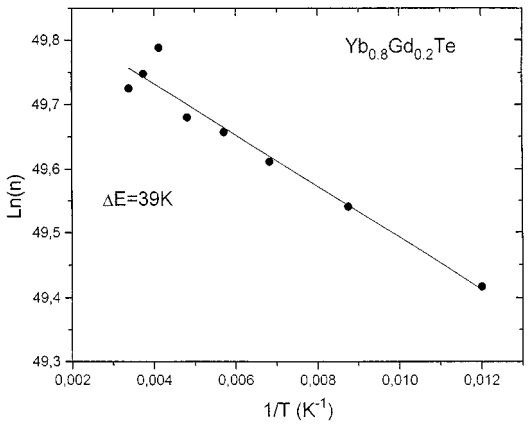

Fig. 16. Logarithm of the electron concentration n expressed in cm^{-3} deduced from the hall constant as a function of the inverse of the temperature in $Yb_{0.8}Gd_{0.2}Te$. The activation energy is $\Delta E = 39$ K.

On another hand, neither the La–Te bond nor the Yb–Te bond depends on x in the solution $Yb_{1-x}La_xTe$ after Figure 13. In particular, the Yb–Te bond length is that of insulating YbTe, even in the range of composition $x > 0.2$ where the solid solution is metallic. The Debye-Waller factor σ_{Te} for the La–Te bond, reported in Figure 15, slowly decreases from 0.075 to 0.06 Å when x increases from 0.3 to 1. σ_{Te} for the Yb–Te bond stays in the range 0.08–0.09 Å for any x from $x = 0$ to $x = 0.8$. Therefore, the invariance of the Yb–Te bond length with x, which contrasts with the situation met in $Yb_{1-x}Gd_xTe$, is not related to smaller thermal fluctuations in $Yb_{1-x}La_xTe$. This is a first evidence that the metal-insulator transition is different in both solid solutions.

5 The insulator-metal transition

Although the IMT takes place at the same concentration $x \approx 0.2$, the transport and the structural properties of $Yb_{1-x}Gd_xTe$ and $Yb_{1-x}La_xTe$ in the vicinity of x_c are different, and we shall analyze them separately.

a) In $Yb_{1-x}Gd_xTe$

The activation energy of the Gd donor in insulating $Yb_{1-x}Gd_xTe$ is small, say 39 K, *i.e.* 3.3 meV in the vicinity of the IMT, after Figure 16. This is the value expected for an hydrogenic level, with enhancement of the binding energy by formation of the bound magnetic polaron. In metallic $Yb_{1-x}Gd_xTe$, transport experiments reveal pretransitional effects in the whole range $0.2 < x < 0.5$ [2–19]. In this prior work, we have evidenced a linear temperature dependence of the electric conductivity in this range of composition, and argued that this strong diffusion regime is dominated by the Coulomb electron-electron interaction, enhanced by magnetic fluctuations *via* the exchange interaction. This different behavior on both sides of $x = 0.5$ is consistent with the analysis of EXAFS data, since the entrance in the critical regime for the IMT, at $x = 0.5$, corresponds to a break in the slope of the nn Yb–Te distance in Figure 16. This is an evidence that the Yb–Te bond is sensitive to localization effects of the electrons introduced by the neighboring Gd donors. In the following, we shall take advantage of this feature by using the less rigid Yb–Te bond as a local probe for the electron state density.

While the nn Yb–Te bond length shows an anomalous behavior at $x = 0.5$, it varies linearly in the range $0 < x < 0.5$, and no singular behavior can be detected at the critical concentration $x_c \approx 0.2$ for the IMT. To the contrary, the lattice parameter determined from the X-ray diffraction pattern does not show any anomaly at $x = 0.5$, while a jump in the slope of $a(x)$ is observed at $x_c = 0.2$ (see Fig. 1). This difference is related to the fact that X-ray diffraction explores the structure averaged at a large scale, while the EXAFS data are a probe of the structure at an atomic scale. As a probe at large scale, the X-ray diffraction pattern is only sensitive to the capacity of the electron to propagate and give a metallic contribution to the bonding. Indeed, the IMT which separates between phases where Gd electrons can (metal) or cannot (insulator) propagate at an infinite scale, does affect the X-ray pattern and the lattice parameter a at x_c. On another hand, the X-ray pattern and a are not sensitive to the entrance in the pretransitional regime, because the system remains metallic on both sides of $x = 0.5$. However, this pretransitional regime in the composition range $0.2 < x < 0.5$ is due to the onset of strong diffusion of the electrons at a local scale, hence an effect on a local probe of the electronic structure such as the EXAFS data and nn distances.

The data in Figure 16 then gives a new enlightenment on the strong diffusion regime studied in reference [19]. At $x > 0.5$, the solution $Yb_{1-x}Gd_xTe$ is metallic with electrons fully delocalized, hence a nn Yb–Te distance comparable to $a_m(YbTe)/2$. The pre-transitional regime corresponds to a regime of strong diffusion of electrons by local potential fluctuations, so that the electron wavefunction is no longer that of a free electron state, but instead it is similar to that of a virtual bound state, giving rise to a non uniform electron density. Although the "wings" of the wavefunction are still sufficient to preserve the metallic character, the resonant scattering of the electron by the local potential affects the electron density in its close vicinity, hence a change in the local probe, *i.e.* the Yb–Te bond length. The transition to the insulating state is driven by a small decrease in the "wings" of the electron wavefunction at the scale of the distance between Gd^{3+} ions, while the perturbation of the wavefunction in the central part is too small to be detected by the local probe. As the donor level associated to Gd ions is close to the conduction band at $x < 0.2$ and merges in the conduction band in the metallic phase, there is a non negligible hybridization between the Gd donor states and the states at the bottom of the conduction band (essentially d-states of the Yb rare earth ion, plus the s-states of the Te ions. This hybridization, which increases with x, and modifies the nature of the bonding, may be the reason why both the Yb–Te and the GdTe distances vary with x, although the x-dependence

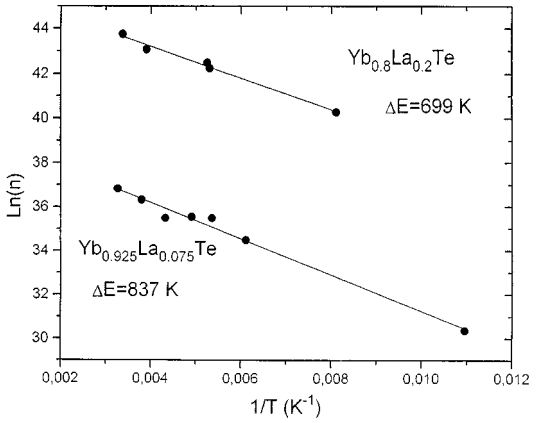

Fig. 17. Logarithm of the electron concentration n expressed in cm^{-3} deduced from the Hall constant as a function of the inverse of the temperature in $Yb_{1-x}La_xTe$ in the insulating phase. ΔE is the activation energy.

is smaller in the case of Gd–Te because this bond is more rigid.

b) In $Yb_{1-x}La_xTe$

The IMT does not show the same features in this solid solution. First, there is no pre-transitional regime. At $x > x_c$, the resistivity curves are characteristics of usual metals, *i.e.* the resistivity is constant at low temperature, then increases when T increases due to the diffusion of free carriers by phonons, according to the Bloch-Grüneisen law. On another hand, the compound at $x < x_c$ is insulating with a very large activation energy E_a for the electrons. For $x = 0.2$, the activation energy according to Figure 17 is 699 K, *i.e.* 58 meV, to be compared with 3.3 meV in $Yb_{1-x}Gd_xTe$ for the same composition. The large value of the activation implies that La cannot be considered as an hydrogenic impurity. A central cell correction to the Coulomb potential plays a key role to turn La a deep level impurity. This central cell correction suggests the d-conduction states of La fall into the gap of YbTe, at an energy far from the bottom of the conduction band of YbTe, so that the hybridization between the Yb and the La states is small.

The rather small variation of the activation energy with x from 58 meV at $x = 0.2$ to 69 meV at $x = 0.075$ suggests that E_a does not extrapolate to zero at x_c. This result, together with the absence of any pre-transitional effect in the resistivity curves suggest that the insulator-metal transition is first order in $Yb_{1-x}La_xTe$.

The absence of any pre-transitional effect also explains that the nn La–Te and Yb–Te distances are independent of x for $0.2 < x < 1$. In this range of compositions where $Yb_{1-x}La_xTe$ is metallic, the nn Yb–Te distance is that of insulating Yb–Te, so that this bond length is actually independent of x in the whole range $0 < x < 1$. This is another major difference with the $Yb_{1-x}Gd_xTe$. This is an evidence that the introduction of La has no sizeable effect on the nn Yb–Te bond length, a result also consistent with the lack of significant hybridization between the Yb and La d-states. The too small contribution of La to EXAF spectra for $x < 0.2$ prevents us from estimating the La–Te bond length in this range, so we could not investigate any effect of the IMT on this length. On another hand, the IMT has an effect on the lattice parameter deduced from X-ray diffraction, just like in the $Yb_{1-x}Gd_xTe$, for the same reasons. The independence of the Yb–Te bond with respect to the La doping suggests that this bond does not participate to the IMT process in $Yb_{1-x}La_xTe$. The metallic conduction of the electrons is then attributable to the motion of the electrons between La ions through the Te anions. This model identifies the IMT in this solid solution as a percolation transition among the LaTe sublattice. As the La atoms are distributed on a fcc lattice, one then expects the IMT takes place at the percolation threshold for this lattice, *i.e.* 0.2, in agreement with the experimental value of x_c. Although the percolation transition is second order in nature, it can be tuned to first order by a driving force. At least, one example of first order percolation transition is provided by orientational glasses [20], in which case the first order is driven by the compressibility. In our case, the first order may come from the dielectric constant which increases with delocalization and weakens the effective localization potential.

6 Conclusion

EXAFS experiments have been achieved to study the effect of electron doping in $Yb_{1-x}Gd_xTe$ and $Yb_{1-x}La_xTe$. In both solid solutions, the distribution of nn rare earth–Te bond length is bimodal, so that the fcc structure is kept only on the average. Local distortions aim to accommodate the presence of two rare earths at the nn sites upon alloying.

The insulator-metal transition (IMT) in $Yb_{1-x}Gd_xTe$ and $Yb_{1-x}La_xTe$ takes place at $x \approx 0.2$ in both solid solutions. The Yb–Te bond length can be used as a probe to investigate the IMT at an atomic scale, which completes previous investigations at a macroscopic scale. This study reveals that the IMT shows different features, despite the fact that the critical donor concentration is the same in both alloys.

A pre-transitional regime is observed in $Yb_{1-x}Gd_xTe$ in the range $0.2 < x < 0.5$. It corresponds to a non uniform electron density due to the presence of resonant potential in a strong diffusion regime, which affects the Yb–Te bond length. The IMT is second order in nature and can be understood as delocalization of the electrons in excess on the Gd donors when their orbital overlap. The shift of the critical concentration with respect to that of the Mott criterium can be attributed to magnetic exchange interactions which shrinks the electron orbital (magnetic polaron effect).

In $Yb_{1-x}La_xTe$, however, no pre-transitional effect is observed, and La donors give rise to deep impurity levels in the insulating phase. The IMT looks first order in nature, and is associated to a percolation transition on the La–Te sublattice. The Yb–Te bond length is almost independent

of x, and close to its value in insulating YbTe, even in the metallic phase ($x > 0.2$).

Beyond the particular cases investigated in this paper, the present work gives evidence that EXAFS experiments are a powerful tool to investigate insulator-metal transitions and related anomalous transport phenomena at a microscopic scale. The limit comes from the fact that EXAFS data are not available for the donor ions in the insulating phase. EXAFS in fluorescence geometry, which is well suited for diluted elements, might be the solution to study the effect of the metal-insulator transition on the bond between donors and nearest neighbors.

References

1. D. Ravot, A. Mauger, J. Alloys and Compounds **178**, 229 (1992).
2. D. Ravot, A. Mauger, O. Gorochov, Phys. Rev. B **48**, 10701 (1993).
3. S. Merah, D. Ravot, A. Percheron-Guégan, J. Olivier-Fourcade, J.C. Jumas, A. Mauger, P. Parent, J. Alloys and Compounds **260**, 17 (1997).
4. A. Balzarotti, N. Motta, A. Kisiel, M. Zimnal-Starnawska, M.T. Czyzk, J. Podgorny, Phys. Rev. B **31**, 7526 (1985); N. Motta, A. Balzarotti, P. Letardi, J. Phys. (Paris) Colloq. **47**, C8-403 (1986).
5. J.K. Furdyna, J. Appl. Phys. **64**, 29 (1988).
6. J. Boyce, J.C. Mikkelsen, Phys. Rev. B **31**, 6903 (1985).
7. H. Sato, T. Yokohama, I. Ono, K. Kaneyuki, T. Ohta, Jpn J. Appl. Phys. **31**, 1118 (1992).
8. A. Frenkel, E.A. Stern, A. Voronel, M. Qian, M. Newville, Phys. Rev. B **49**, 11662 (1994).
9. A. Yoshiasa, F. Kanamaru, S. Emura, K. Koto, Solid State Ion. **27**, 267 (1988).
10. T. Yokoyama, F. Takamatsu, K. Seki, K. Miyake, T. Tani, T. Ohta, Jpn J. Appl. Phys. **29**, L1486 (1990).
11. Y.T. Tan, K. Lushington, J. Phys. Chem. Solids **54**, 309 (1993).
12. A. Michalowicz, in *Logiciels pour la chimie* (Édition Française de Chimie, Paris, 1991), p. 102; V. Voinville, A. Michalowicz, A. Galaad, in *Logiciels pour la chimie* (Édition Française de Chimie, Paris, 1991), p. 116.
13. D. Bonnin, P. Kaiser, C. Frétigny, J. Desbarres, *Structures fines d'absorption des rayons X en chimie*, École du CNRS Orsay-Garchy (1989), to be published in *Proceedings of the 10th Int. Conf. on XASF*, Aug. 1998, Chicago (USA).
14. B.K. Teo, P.A. Lee, J. Am. Chem. Soc. **11**, 101 (1979)
15. A.G. Mc Kale, B.W. Veal, A.P. Paulikas, S.K. Chan, G.S. Knapp, J. Am. Chem. Soc. **110**, 3763 (1988).
16. P.A. Lee, P.H. Citrin, P. Eisemberg, B.M. Kincaid, Rev. Mod. Phys. **53**, 769 (1981).
17. J.C. Mikkelsen, J.B. Boyce, Phys. Lett. **49**, 1412 (1982); Phys. Rev. B **28**, 7130 (1983).
18. See, for example, A. Mauger, C. Godart, Phys. Rep. **141**, 51 (1986).
19. D. Ravot, A. Mauger, O. Gorochov, Europhys. Lett. **24**, 65 (1993).
20. S. Galam, Europhys. Lett., in press.